UC Santa Barbara
UC Santa Barbara Previously Published Works

Title

Resonant Soft X-ray Scattering Reveals the Distribution of Dopants in Semicrystalline Conjugated Polymers.

Permalink

https://escholarship.org/uc/item/0gm2n0nj

Journal

The Journal of Physical Chemistry B (Soft Condensed Matter and Biophysical Chemistry), 128(50)

Authors

Nguyen, Phong

Callan, Devon

Plunkett, Evan

et al.

Publication Date

2024-12-19

DOI

10.1021/acs.jpcb.4c05774

Peer reviewed

Article

Resonant Soft X-ray Scattering Reveals the Distribution of Dopants in Semicrystalline Conjugated Polymers

Published as part of The Journal of Physical Chemistry B special issue "Mark Ediger Festschrift".

Phong H. Nguyen, Devon Callan, Evan Plunkett, Max Gruschka, Nima Alizadeh, Matthew R. Landsman, Gregory M. Su, Eliot Gann, Christopher M. Bates, Dean M. DeLongchamp,* and Michael L. Chabinyc*

Read Online

ACCESS | Metrics & More | Article Recommendations | SI Supporting Information

ABSTRACT: The distribution of counterions and dopants within electrically doped semicrystalline conjugated polymers, such as poly(3-hexylthiophene-2,5-diyl) (P3HT), plays a pivotal role in charge transport. The distribution of counterions in doped films of P3HT with controlled crystallinity was examined using polarized resonant soft X-ray scattering (P-RSoXS). The changes in scattering of doped P3HT films containing trifluoromethanesulfonimide ($TFSI^-$) and 2,3,5,6-tetrafluoro-7,7,8,8-tetracyanoquinodimethane ($F_4TCNQ^{\bullet-}$) as counterions to the charge carriers revealed distinct differences in their nanostructure. The scattering anisotropy of P-RSoXS from doped blends of P3HT was examined as a function of the soft X-ray absorption edge and found to vary systematically with the composition of crystalline and amorphous domains and by the identity of the counterion. A computational methodology was developed and used to simulate the soft X-ray scattering as a function of morphology and molecular orientation of the counterions. Modeling of the P-RSoXS at N and F K-edges was consistent with a structure where the conjugated plane of $F_4TCNQ^{\bullet-}$ aligns perpendicularly to that of the P3HT backbone in ordered domains. In contrast, $TFSI^-$ was distributed more uniformly between domains with no significant molecular alignment. The approach developed here demonstrates the capabilities of P-RSoXS in identifying orientation, structural, and compositional distributions within doped conjugated polymers using a computational workflow that is broadly extendable to other soft matter systems.
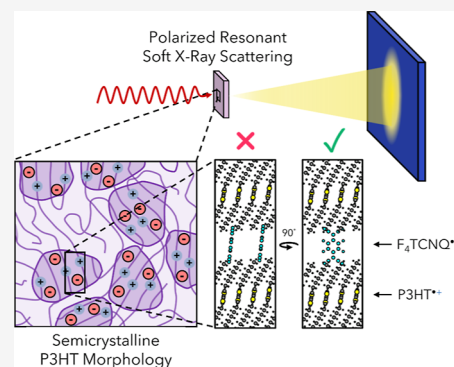
1. INTRODUCTION

Electrical doping of conjugated polymers introduces charge carriers and adjacent dopants or counterions.[1] Understanding the interplay between charge carriers—often localized as polarons—and counterions across local structural regions is essential for optimizing the transport properties of these materials.[2−4] One primary challenge is determining how the charge carriers and counterions are distributed across these regions of the polymer after infiltration during the doping process. This infiltration is influenced by mass transport, which is governed by free volume and polymer segmental dynamics, suggesting that counterions are likely more readily transported through disordered, amorphous domains than in ordered, crystalline domains.[2] The electronic charge carriers are expected to have higher mobility in ordered domains, and thus it is crucial to understand the distribution of counterions and charge carriers postdoping. Here, we focus on the distribution and organization of counterions trifluoromethanesulfonimide ($TFSI^-$) and 2,3,5,6-tetrafluoro-7,7,8,8-tetracyanoquinodimethane ($F_4TCNQ^{\bullet-}$) within these crystalline and amorphous domains in a model doped conjugated polymer, poly(3-hexylthiophene) (P3HT).

Given the low dielectric constant ($2 < \varepsilon_r < 4$) of typical polymers, long-range electrostatic interactions between the charge carriers and counterions from doping are prevalent. These interactions lead to electrostatic trapping of charge carriers by their associated counterion causing the carrier mobility to depend on the charge concentration.[5] The Bjerrum length—where electrostatic and thermal energies balance—ranges from (14 to 30) nm at room temperature in conjugated polymers. The center-to-center distance of crystalline domains in P3HT is ≈20 nm and comparable to this electrostatic length scale.[6−8] This overlap implies that electrostatic interactions, carrier concentration, and microstructure are key factors in charge transport.[5] At high average charge carrier densities ($\approx 10^{20}$ cm^{-3}), which lead to high electrical conductivity in polymers, screening effects can alter the interactions between
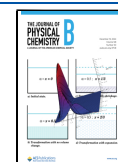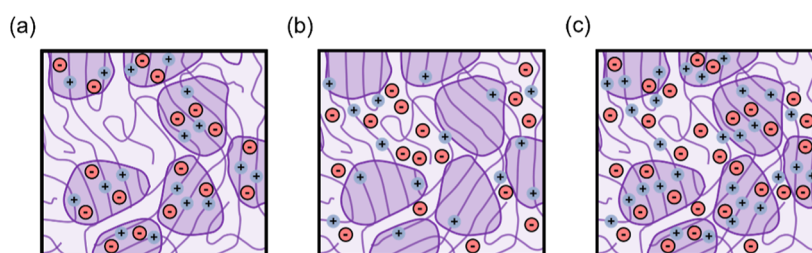
Figure 1. Schematic of hypothetical distributions of doping of a semiconducting polymer, including positive charge carriers and their negatively charged counterions localized within (a) crystallites, (b) amorphous regions, and (c) distributed uniformly between them.
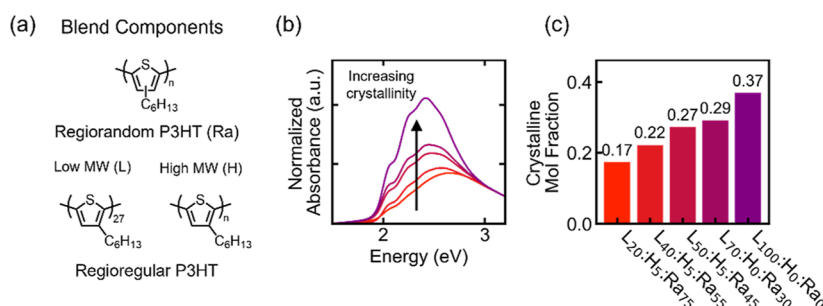
Figure 2. (a) Regiorandom (RRa) and regioregular (RRe) P3HT of varying molecular weights were blended to control the total degree of crystallinity. (b) UV−vis absorbance spectra of a series of blends showing increased vibronic absorbance with increasing RRe P3HT. (c) Mole fraction of crystalline P3HT blends corresponding to spectra shown in (b). The compositions of each blend is specified using $L_x:H_y:Ra_z$, with x being the mole percent of low molecular mass RRe P3HT, y being the mole percent of high molecular mass P3HT, and z representing the mole percent of RRa P3HT.

carriers and counterions in addition to their distribution across ordered and disordered polymer domains. Direct measurements of the nanostructure are essential to help understand these interactions.

Recent work has shown a correlation between structural disorder and electrical conductivity at high carrier concentrations rather than electrostatic effects alone.[4] Contrary to initial expectations, ion size—a factor coupled to electrostatic trapping—plays a subordinate role compared to the effect of structural order.[3,4] Doping can lead to planarization of the backbone of the conjugated polymer and increased structural order overall.[9−11] A dependence of structural order on the level of doping further complicates this picture. For example, the ratio of polymer repeat units to carriers can range from $\approx 4 \times 10^5$ at low doping levels (10^{16} carriers·cm^{-3}) to as low as ≈ 4 at high doping levels (10^{21} carriers·cm^{-3}). Consequently, the average distance between counterions can vary from as high as 45 nm to as low as ≈ 1 nm. Fluctuations from these average distances can arise from doping that is localized within either crystalline or amorphous domains. Additionally crystalline domains in p-type polymers are more readily doped via integer charge transfer with dopants due to their lower barrier to ionization, whereas amorphous domains may preferably form charge transfer complexes with some dopants.[12−14] This distinction in charge transfer mechanisms has significant implications for the electronic transport properties of doped films. Thus, a comprehensive understanding of structural disorder and dopant distribution are necessary for optimizing the macroscopic charge transport properties.

While there have been notable advancements in understanding dopant distribution in conjugated polymers, current methodologies often focus on either crystalline or amorphous domains, not both, limiting a comprehensive understanding of dopant distribution. Wide angle hard X-ray scattering excels in probing changes within the crystallites of conjugated polymers, yet cannot provide detail about amorphous domains.[15,16] Conversely, electrochemical strain microscopy offers valuable insights on swelling behavior, particularly in amorphous domains.[17,18] The insights gained to date are relatively consistent, showing a preference for dopants to localize within either crystalline or amorphous domains depending on the structure of the semiconducting polymer. These range from highly crystalline polymers, like the thienothiophene-based polymer poly[2,5-bis(3-tetradecylthiophen-2-yl)thieno[3,2-*b*]-thiophene] (PBTTT), to those engineered for enhanced polarity to incorporate ions, such as the oligoether side chain-functionalized polythiophene poly(3-[2-(2-methoxyethoxy)-ethoxy]methylthiophene-2,5-diyl) (P3MEEMT).[13,18−29] The differences between materials depend on factors including the relative redox potentials of polymer domains and dopants, as well as dopant counterion chemistry and size. Despite the significant body of work correlating structural changes in conjugated polymers to doping,[18] a comprehensive perspective integrating both domain types, along with dopant identity and levels, is still lacking. Considering these observations, our approach aims to study dopant distributions simultaneously across both crystalline and amorphous regions in a single material and as a function of dopant identity.

We employed polarized resonant soft X-ray scattering (P-RSoXS) to examine the nanostructure of doped P3HT films, leveraging its unique contrast modalities based on elemental composition, bond presence, and bond orientation. While P-RSoXS offers rich insights, its quantitative interpretation is greatly assisted in complex systems with forward simulation computational methods.[30−35] Using P3HT as a model system, we outline a workflow for simulating P-RSoXS and its application in resolving the distributions of counterions with two distinct chemical structures in doped P3HT films. We
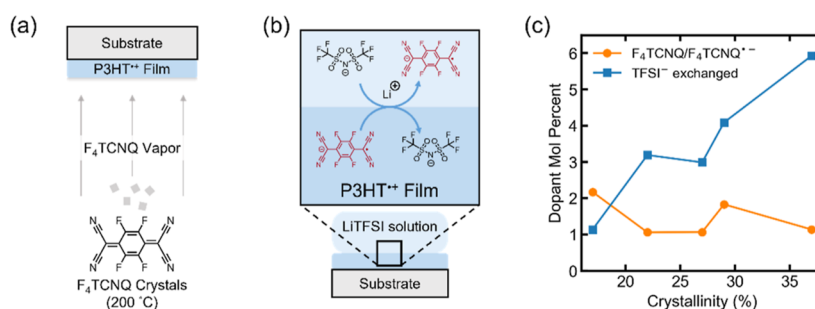
Figure 3. (a) Schematic depiction of the F_4TCNQ vapor doping process, where F_4TCNQ crystals are sublimated onto a P3HT film, achieving uniform doping, and depositing a small excess of neutral F_4TCNQ on top. (b) Schematic depiction of the ion-exchange process to exchange $TFSI^-$ into the P3HT blend containing $F_4TCNQ^{\bullet-}$ using a LiTFSI solution. (c) Dopant concentration (relative to P3HT repeat units) in the middle of the film measured by XPS versus the crystallinity of the film.

developed a model system using blends of P3HT that allowed us to control the size and concentration of ordered domains and a computational real-space analogue for simulation. The model allowed us hypothesis-test different polymer–dopant orientations and distributions. Our analysis, supported by complementary techniques, isolates the effects of various hypothetical distributions of doping, such as those schematically drawn in Figure 1, providing a clearer understanding of the structure of doped polymers. This integrated approach not only reveals that the distribution of doping can vary depending on the molecular geometry of the counterion but also suggests preferential orientations of the counterion relative to P3HT crystallites. This information provides a roadmap for future studies to consider orientation-dependent phenomena such as charge transfer.

2. EXPERIMENTAL AND COMPUTATIONAL METHODS

Certain commercial equipment, instruments, software or materials, commercial or noncommercial, are identified in this paper in order to specify the experimental procedure adequately. Such identification does not imply recommendation or endorsement of any product or service by National Institute of Standards (NIST), nor does it imply that the materials or equipment identified are necessarily the best available for the purpose.

2.1. Materials and Processing Conditions. Low number-average molecular mass regioregular (RRe) P3HT [4.5 kg/mol, dispersity ($Đ$) = 1.6], high molecular mass RRe P3HT (23 kg/mol, $Đ$ = 1.8), and regiorandom (RRa) P3HT (16.3 kg/mol, $Đ$ = 2.5) (Figure 2), were dissolved in an equal-volume mixture of chlorobenzene and dichlorobenzene. P3HT solutions of varying blend composition were drop cast onto substrates to form (700 to 1000) nm thick films. P3HT films were doped in an inert nitrogen glovebox atmosphere, enclosing the film and ≈3 mg of F_4TCNQ crystals within a jar in the orientation depicted in Figure 3.[36] The jar was heated to 200 °C for 45 min, allowing for sublimation of F_4TCNQ to oxidize the P3HT film. $TFSI^-$-containing samples were formed by anion exchange from immersion in a concentrated LiTFSI solution (0.03 mass fraction in acetonitrile) for 120 min at 60 °C. Error! Reference source not found. Table S1 summarizes the varying P3HT blend compositions utilized in this study, resultant levels of aggregation, and dopant counterion concentrations.

2.2. Atomic Force Microscopy. An Asylum MFP-3D atomic force microscope was used in tapping mode to examine the surface roughness of the P3HT blend films. The AFM tip was a silicon cantilever with a resonance frequency of approximately 61 kHz and a spring constant of about 1.6 N/m (Figure S1).

2.3. UV–Vis Absorbance Spectroscopy. All ultraviolet–visible (UV–vis) spectra were acquired using an Agilent Technologies Cary 60 UV–vis spectrometer. Samples were drop cast from solution onto quartz substrates to form optically transparent films. Spectra for P3HT films of varying composition were fit to the Spano model via a custom Python script to quantify aggregate mole fractions.[37–39]

2.4. X-ray Photoelectron Spectroscopy. X-ray photoelectron spectroscopy (XPS) measurements were performed using an Escalab Xi+ Spectrometer from ThermoFisher Scientific. The spectrometer operated under a high vacuum condition of 10^{-6} Pa and utilized a monochromatic aluminum $K\alpha$ X-ray source. To stabilize charge during the measurements, we used a dual ion-electron low-energy flood source. For acquiring survey spectra, we set the pass energy to 100 eV and conducted five scans at intervals of 0.25 eV, each with a dwell time of 50 ms. Depth profiling was done using an ion gun with a 1000-atom Ar^+ cluster and an ion energy of 6000 eV. Ion sputtering covered a square region measuring (1.5×1.5) mm^2. Within this area, we collected photoexcited electrons from the inner (400×400) μm^2 region to selectively isolate signal from crater centers. All spectra are presented in the Supporting Information along with an AFM images of the topography of the films (Figures S2–S6).

2.5. Grazing Incidence Wide Angle X-ray Scattering. Grazing incidence wide-angle X-ray scattering (GIWAXS) was performed at the BioPACFIC MIP user facilities at UC Santa Barbara and experimental station 11-3 at the Stanford Synchrotron Radiation Lightsource. Angle-resolved GIWAXS scans were acquired with 120 s exposures at grazing incidence angles of 0.05°, 0.10°, and 0.13° using an X-ray energy of 12.7 keV. 2D detector images were remapped to q-space using Nika[40] or GIWAXS_Tools. Partial pole figure analysis was done using a custom open-source python package (https://github.com/phonghnguyen/GIWAXS_Tools). See Figures S7–S9 in Supporting Information for more details of the analysis and representative partial pole figures used for model morphology development.

2.6. Resonant Soft X-ray Scattering. Polarized resonant soft X-ray scattering (P-RSoXS) experiments were performed at the Spectroscopy Soft and Tender (SST-1) beamline funded and operated by the National Institute of Standards and Technology (NIST) at the National Synchrotron Light Source

II (NSLS-II).[41] Data reduction was performed using PyHyperScattering (https://github.com/usnistgov/PyHyperScattering), an open source package for hyperspectral scattering reduction and analysis.[42] Thin film samples on transparent silicon nitride windows were mounted normal to the incident X-ray beam with samples measured in transmission mode under high vacuum conditions.

2.7. Computation of Near Edge X-ray Absorption Fine Structure. Near edge X-ray absorption fine structure (NEXAFS) simulations were carried out using the PWscf and XSpectra software packages of the Quantum ESPRESSO distribution.[43−47] The simulation process consists of (1) sourcing equilibrated or equilibrating atomic coordinates for a given molecule,[48] (2) obtaining the electronic structure for each core-hole configuration of the molecule, and (3) calculating the polarization-dependent X-ray absorbance spectra for each core-hole configuration. The configuration-specific spectra are offset by their relative total energies. The sum of spectra for each polarization direction are offset to experimental absorption onsets (e.g., the C 1s → $\pi^*_{C=C}$ peak measured at 285.25 eV) to obtain oriented NEXAFS (Figures S10−S23). The NEXAFS are normalized to the bare atom scattering factors to obtain the imaginary component of the refractive indices, β, which can be used to solve for the real portion, δ, using the Kramers−Kronig relations.[49,50]

To calculate P3HT NEXAFS, atomic coordinates for unit cells of low-energy crystalline polymorphs of P3HT were sourced from literature.[48,51] We adopt the approach of using a supercell consisting of 3-hexylthiophene 8-mer with periodic boundary conditions to represent a single polymer chain.[48,51] This is consistent with prior work demonstrating that 6 repeat units is sufficient to isolate adjacent core-hole excitons.[52] Our tests also confirmed that π-stacking effects are minimal and that k-point sampling density variations produce negligible spectral changes (Figures S10−S13). This further confirms that the chosen supercell is sufficient to capture key attributes of the simulated NEXAFS.

For the simulations involving dopant counterions, atomic coordinates were geometrically optimized through a relaxation calculation in Quantum ESPRESSO. A single dopant molecule within a sufficiently large cubic lattice was used to ensure the isolation of core-hole exciton effects. The optimization process employed the generalized gradient approximation (GGA), following the Perdew−Burke−Ernzerhof (PBE) scheme, and utilized a plane-wave cutoff energy of 30 Ry. Corroborative X-ray absorbance spectra and comparisons with experimental results are provided in the Supporting Information (Figures S24−S33).

2.8. P-RSoXS Simulations. P-RSoXS simulations were carried out using the NIST RSoXS Simulation Suite (NRSS) which incorporates tools to validate input models and CyRSoXS, a virtual beamline instrument.[32] Simulated morphologies were generated using a custom software (https://github.com/devoncallan/DopantModeling).

3. RESULTS AND DISCUSSION

3.1. Doping of P3HT Films with Controlled Crystallinity. Our goal is to understand how dopants or counterions are distributed between ordered and disordered regions in a model conjugated polymer. The charge carrier in a conjugated polymer results from an electron−transfer reaction between a neutral segment of the polymer and a dopant. The dopant may remain in the semiconducting polymer as the counterion that

balances the charge carrier or it can be exchanged for a different counterion. Figure 1 presents a schematic representation illustrating hypothetical distributions of resultant counterions between crystalline and amorphous phases in the case of p-doping. For P3HT, the crystallites have the smallest ionization energy and are more readily oxidized than the amorphous regions.[9,53] With a relatively weak dopant like F_4TCNQ there is likely to be a preference for doping of ordered domains. This understanding guided our choice of a model system that would allow us to control the ordered and disordered regions in a semiconducting polymer, thereby enabling an in-depth analysis of how counterions distribute between these domains using various methods.

We chose a model system based on blends of regioregular (RRe) and regiorandom (RRa) P3HT. Low molecular weight RRe P3HT (4.5 kg/mol) was chosen to be below the contour length of the high molecular weight RRe P3HT (23 kg/mol) in the blend.[54,55] This choice sets the nominal diameter of fibrillar crystals formed by the low molecular weight P3HT chains, confirmed via atomic force microscopy (see Figure S1). The minor amount of high molecular weight RRe P3HT facilitates connections between crystallites, with the remainder of the blend composition consisting of RRa P3HT. The range of blends from 0.25 to 1.0 mass fraction RRe P3HT was selected to systematically vary the degree of crystallinity. We used UV−vis absorbance spectra to estimate the mole fraction of crystalline to amorphous P3HT as the mole fraction of aggregates, ranging between approximately 0.2 and 0.4 mole fraction (see Figure 2).[37] Notably, the ratio of H to J aggregates remained consistent across blends, reinforcing that the blend composition primarily influences the fraction of aggregates rather than the structural type of aggregation. Table S1 summarizes the varying P3HT blend compositions utilized in this study and the resultant levels of aggregation.

To investigate how counterions distribute in electronically doped blends of P3HT, we chose two structurally dissimilar dopants. Initially, F_4TCNQ vapor was applied to dope the P3HT blend. The counterion in the doped film was subsequently changed using an anion exchange process with a LiTFSI solution that removes the initial counterion $F_4TCNQ^{\bullet-}$ (see Figure 3). F_4TCNQ is nominally planar and possesses a conjugated structure, similar to P3HT, creating the possibility of preferential orientation or location within the unit cell of crystalline domains.[13,16,20−22,27] In contrast, $TFSI^-$ is nonplanar with multiple conformers, leading to a different set of interactions and no expectation of preferential orientation relative to P3HT.

3.2. Dopant Uptake with Varying Crystallinity and Counterion Identity. We verified that the doping was uniform throughout the depth of the P3HT blend films before and after ion exchange. We utilized XPS in conjunction with ion sputtering to analyze the concentration throughout the film depth of F_4TCNQ after doping and $TFSI^-$ after ion exchange. The analysis spot size, here (400×400) μm^2, does not offer detailed lateral spatial resolution; instead, it gives a lateral average view of the relative dopant concentrations. Our XPS and ion sputtering analyses revealed consistent dopant distribution throughout the entire depth of P3HT films doped with F_4TCNQ, and a nearly complete transition to $TFSI^-$ after prolonged immersion in LiTFSI solution, as detailed in Figures S2−S4.

Interestingly, while the concentration of $F_4TCNQ/F_4TCNQ^{\bullet-}$ remained relatively consistent across different
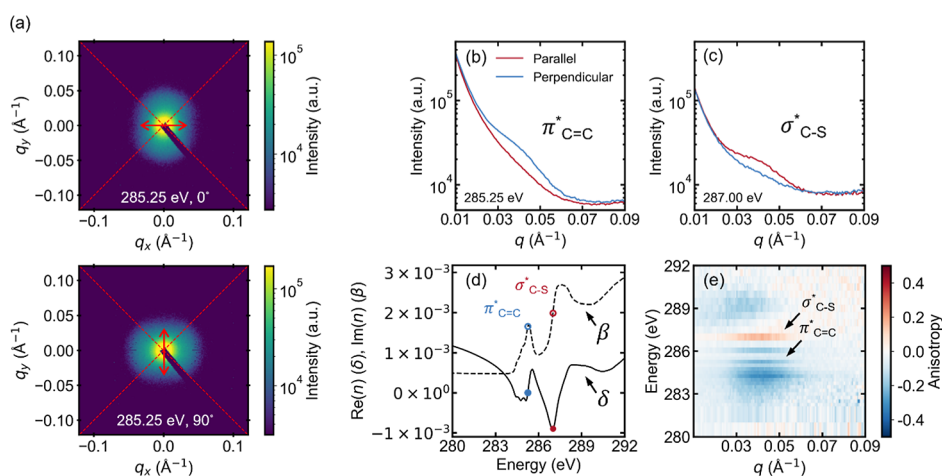
Figure 4. (a). X-ray detector images from a 37% crystalline P3HT blend film using 285.25 eV X-rays, changing only X-ray polarization between 0° (top) and 90° (bottom). The dashed red lines separate 90° arcs over which scattering was integrated for directions parallel or perpendicular to the X-ray electric field polarization direction (denoted by the red double-headed arrow). Integrated scattering intensity (within 90° arcs) parallel and perpendicular to the X-ray polarization, showing inversions of scattering anisotropy at (b) 285.25 eV and (c) 287 eV. (d) These energies are correlated with the C 1s → $\pi^*_{C=C}$ and C 1s → σ^*_{C-S} transition energies as indicated in the isotropic P3HT refractive indices. (e) Anisotropy of scattering across energies and q shows features at transition energies associated with the refractive indices in (d).

blend compositions and levels of film crystallinity, we observed an increase in TFSI⁻ concentration correlating with greater film crystallinity. A potential explanation is the incorporation of excess neutral LiTFSI, along with TFSI⁻ to replace $F_4TCNQ^{\bullet-}$, but XPS analysis reveals only negligible amounts of Li⁺ in the samples most rich in TFSI⁻ (refer to Figure S2). Instead, atomic force microscopy (AFM) measurements of doped films (see Figure S5) indicate an increase in phase contrast following F_4TCNQ vapor doping, which we attribute to the deposition of excess neutral F_4TCNQ. Subsequent anion exchange in LiTFSI solution appears to reduce the phase contrast in AFM. Our estimates for a 1000 nm thick film with 0.059 mole fraction TFSI⁻ (0.096 volume fraction, based on a doped film density of 1.1 g/cm³) and 0.011 mole fraction $F_4TCNQ^{\bullet-}$ (0.019 volume fraction) suggest an ≈50 nm layer of excess F_4TCNQ (1.6 g/cm³ bulk density) distributed about the film surface, which has an average roughness of ≈25 nm. Our estimates of a F_4TCNQ top layer are further corroborated by XPS measurements (Figure S6). We propose that presence of excess F_4TCNQ provides the necessary oxidant to allow for greater incorporation of TFSI⁻ via ion exchange doping as observed in literature.[25,56,57]

3.3. P-RSoXS Scattering Anisotropy as a Measure of Morphology and Molecular Orientation. We characterized the nanostructure of the P3HT blends before and after doping using P-RSoXS. We observe energy-dependent changes to the 2D scattering profile due to variations in the anisotropic index of refraction. Contributions to energy-dependent scattering intensity can include vacuum contrast due to heterogeneity in density or sample roughness, material contrast due to compositional heterogeneity, and orientational contrast due to bond orientation heterogeneity. Orientational contrast in P-RSoXS arises due to the spatial variation of the resonant transition dipole orientation interacting with the fixed incident soft X-ray electric field vector. Soft X-ray absorbance is proportional to the dot product of the electric field vector and the transition dipole, which leads to variation in both the imaginary and real components of the complex anisotropic indices of refraction with molecular orientation.[30,58,59] In many systems, the molecular orientation is preferentially relative to

specific aspects of the form factor of a scattering object (preferentially tangential or radial relative to the object surface, preferentially parallel or perpendicular to object long axes, etc.), and in these systems, orientational contrast can give rise to P-RSoXS patterns that are anisotropic, and in which the direction of anisotropy is dependent on the electric field vector orientation (polarization).

We observe such anisotropic patterns in the 2D scattering profiles on the left side of Figure 4, which show scattering from an undoped P3HT blend film by polarized 285.25 eV X-rays, an energy at which the optical properties are strongly influenced by the P3HT C 1s → $\pi^*_{C=C}$ transition dipole moment. Both detector images were captured for the same sample (undoped 37% crystalline P3HT) in the same position and orientation, changing only the direction of X-ray polarization. The fact that high-q scattering follows the X-ray electric field polarization indicates that the scattering anisotropy is due to correlations of molecular orientation with specific aspects of the scattering object. This spatial frequency is related to a combination of fibril form-factor scattering and a long period.[8,35] Distinguishing the dominant factor would require analysis of multiple peak orders; here, we observe only a single peak the range of 0.01−0.1 Å⁻¹ (6.3 to 63 nm).[33,59] Our observations of scattering anisotropy for undoped P3HT are consistent with prior measurements with maxima near 0.04 Å⁻¹ and an inversion from negative to positive scattering anisotropy at 287 eV.[35]

The sensitivity of scattering anisotropy to the real and imaginary portions of the index of refraction ($n = 1 − \delta + i\beta$) and the alignment between different transition dipole moments and X-ray polarization is made clear when comparing the scattering at different resonant energies that correspond to orthogonal transition dipole moments. For example, the C 1s → σ^*_{C-S} transition dipole moment at 287 eV is predominantly parallel to the plane of a thiophene ring, whereas the C 1s → $\pi^*_{C=C}$ transition dipole moment at 285.25 eV is predominantly perpendicular to that plane.[31,52] Preferential orientation in P3HT thus causes the directions of scattering anisotropy at 285.25 and 287 eV to be opposite, though we caution that there is no expectation of a strict correlation
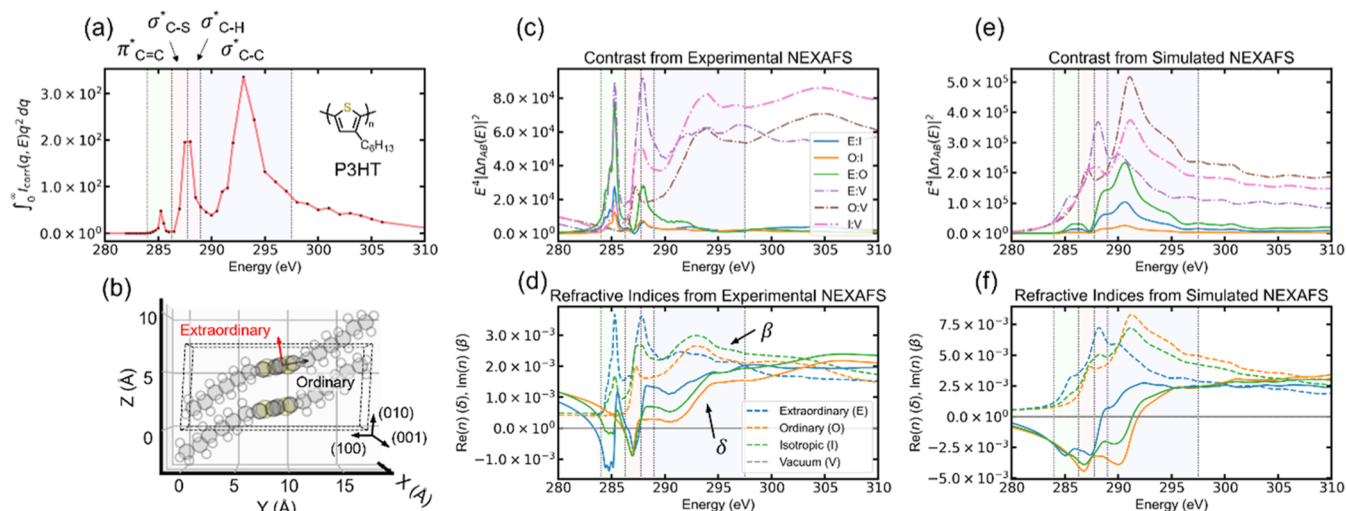
Figure 5. (a) Integrated scattering intensity as a function of X-ray energy, with shaded regions indicating the energies corresponding to the C 1s → $\pi^*_{C=C}$, σ^*_{C-S}, σ^*_{C-H}, and σ^*_{C-C} transitions. A 3D representation of the P3HT unit cell is depicted in (b), where directional arrows denote the extraordinary axis (red) associated with the C 1s → $\pi^*_{C=C}$ transition dipole moment, and the ordinary axes (black). Semitransparent atoms represent hydrogen (white), carbon (gray), sulfur (yellow), and the dashed outline indicates the boundaries of the unit cell. (c) The contrast derived from experimental refractive indices data. (d) Experimental refractive indices of P3HT, with X-ray electric field polarization aligned along the extraordinary (E) axis, ordinary (O) axes, isotropic (I) configuration (unaligned), and vacuum (V) conditions. (e) Simulated refractive indices of P3HT, with the real and imaginary parts presented similarly to the experimental results in (d).

between NEXAFS isosbestic points and P-RSoXS anisotropy direction because NEXAFS depends only on β whereas P-RSoXS depends on both β and δ. To quantify scattering anisotropy across energies, E, and q, we use the definition of scattering anisotropy in eq 1.[30,35,58]

$$A(q, E) = \frac{I_{\parallel}(q, E) - I_{\perp}(q, E)}{I_{\parallel}(q, E) + I_{\perp}(q, E)} \tag{1}$$

In eq 1, $A(q, E)$ is the scattering anisotropy, $I_{\parallel}$ is the integrated scattering intensity about a 90° wedge centered along the X-ray polarization direction, and $I_{\perp}$ is the integrated scattering intensity about a 90° wedge centered 90° from the X-ray polarization direction. As such, $A(q, E)$ quantifies scattering anisotropy induced by the applied electric field vector, capturing aspects of the length scales of the morphology (inherited from X-ray scattering) and molecular orientation (imparted by polarization of the incident X-ray electric field). We note that the value of $A(q, E)$ will depend on angular width of the wedge. The choice of 90° is natural for systems in which the lowest degree of rotational symmetry in the collected RSoXS pattern is 180° rotational symmetry, as is most commonly observed and we observe in our own data, and it further maximizes the ratio of signal-to-noise in $A(q, E)$. Although the analysis of $I(q, E)$ is frequently valuable for understanding P-RSoXS data, we find in this work that $A(q, E)$ includes sufficient contributions from vacuum contrast and materials contrast such that it can be used exclusively to understand and model the P-RSoXS data. We later show, both experimentally and from simulation, that $A(q, E)$ in doped films is related to the counterions and their orientation, allowing us to discern dopant distribution from hypothesized models.

3.4. Fibrillar Crystals and Orientational Self-Contrast in P-RSoXS. Scattering anisotropy alone is a difficult metric to interpret because it combines information about electronic transitions within the material, spatial correlations, and the orientation of transition dipole moments relative to the X-ray

polarization. Studies of scattering anisotropy in undoped conjugated polymers have led to a robust understanding that orientational correlations between aligned domains can contribute to anisotropic scattering within P-RSoXS. For example, previous studies involving blends of P3HT with relatively isotropic $PC_{61}BM$, a fullerene-based material used in organic photovoltaics, have demonstrated that molecular alignment correlated with the domain shape and spatial distribution produces anisotropic scattering patterns.[60] For many semicrystalline conjugated polymers, a principal source of scattering anisotropy is the C 1s → $\pi^*_{C=C}$ transition dipole, which disrupts isotropic symmetry at the molecular level along the direction normal to the conjugated plane of the polymer backbone.[35,61,62] Sensitivity to this dipole has facilitated differentiation between various types of fibrillar crystallites, where the alignment between the fibril long axis and the C 1s → $\pi^*_{C=C}$ transition dipole moment may vary.[35]

To determine sources of scattering contrast, it is helpful to analyze the integrated scattering intensity (ISI) as a function of energy. Because the ISI represents a weighted sum of binary contributions, this analysis allows us to distinguish the dominant factors in the measured scattering contrast.[30] The integrated scattering intensity as a function of incident X-ray energy, $Q(E)$, defined in eq 2.

$$Q(E) = \int_0^{\infty} I_{corr}(q, E) q^2 \, dq \tag{2}$$

In eq 2, $Q(E)$ is the energy-dependent Porod invariant [approximated with the ISI in Figure 5] and I_{corr} is the absorbance-corrected scattering intensity, which accounts for diminished scattering intensity as a function of absorbance through the sample thickness, q, and energy-dependent absorbance. Details on absorbance correction can be found in the Supporting Information. $Q(E)$ can be interpreted as the Lorentz-corrected scattering across all q and thus represents the total population of scatterers as a function of incident X-ray energy. In hard X-ray scattering, $Q(E)$ arises from differences

in electron density between different phases/components. Within P-RSoXS, a chemically homogeneous sample with anisotropic refractive indices can be treated similarly with each orientation (possessing orientation-dependent X-ray refractive indices) treated essentially as a different phase. To aid the initial identification of the predominant binary contrast, we consider hypothetical binary systems for which $Q(E)$ is proportional to the binary contrast, $E^4[(\delta_A(E) - \delta_B(E))^2 + (\beta_A(E) - \beta_B(E))^2]$, with δ_i and β_i being the real and imaginary components of the complex refractive indices.[63] We note that accurate measurements of $Q(E)$ require filtering of fluorescence background. To accomplish this, we fit a power-law scattering form factor at high q and subtracted the constant offset to remove signals of isotropic fluorescence.[64] All experimental results presented have been corrected for absorbance and isotropic fluorescence. We note that while corrections for absorbance and fluorescence are critical for the analysis of absolute scattering intensity, scattering anisotropy is unaffected due to its differential nature. We later focus on simulated and experimental scattering anisotropy to interpret dopant spatial and orientational distributions.

In Figure 5, we show the measured ISI, an approximation of $Q(E)$, with experimentally extrapolated and directly simulated P3HT X-ray refractive indices. The uniaxial optical tensor approximation was used to define the system; the normal to the thiophene plane (corresponding to the C 1s → $\pi^*_{C=C}$ transition dipole moment) is defined as the extraordinary axis, and refractive indices along the two orthogonal axes are averaged to represent the refractive indices in any direction parallel to the conjugated plane (ordinary axis). This approach highlights that the scattering at energies below 290 eV is dominated by the C 1s → $\pi^*_{C=C}$ followed by the C 1s → σ^*_{C-S} transitions, suggesting that the source of this scattering is orientational self-contrast.[6] We note that C 1s → σ^*_{C-H} transitions contribute to the higher energy portion of the peak centered near 288 eV and that the peak centered near 293 eV corresponds to C 1s → σ^*_{C-C} transitions, both from the hexyl side chain of P3HT (see Figure S12).

We employ both experimental data and direct simulations of P3HT NEXAFS to determine the optical properties of P3HT.[60] C 1s NEXAFS of P3HT, experimentally extrapolated to the extraordinary and ordinary axes, were obtained from literature.[6,59,65,66] Briefly, isotropic P3HT NEXAFS of spun-cast films were obtained at the "magic" angle of 54.7°, balancing contributions of in-plane and out-of-plane preferential alignments. By comparing differences between the isotropic P3HT NEXAFS and that measured at normal incidence, the NEXAFS could be extrapolated to the point where the $\pi^*_{C=C}$ resonance disappears (where the X-ray electric field polarization is assumed to be aligned within the ordinary plane) and extrapolated toward perfect 1s → $\pi^*_{C=C}$ transition dipole alignment with the extraordinary axis. The simulated NEXAFS are obtained by directly simulating X-ray electric field polarizations aligned with and orthogonal to the extraordinary axis. Note that the extraordinary axis is slightly tilted from the (010) direction within the P3HT unit cell (see Figure 5b). These simulated and experimentally extrapolated NEXAFS were normalized to bare atom scattering factors from the Henke database and transformed using the Kramers–Kronig relations. The resulting β and δ are shown in Figure 5d,f, respectively.[49,50] At the N and F K-edges, the expected β for P3HT were calculated from the bare-atom scattering

factors and δ was calculated using the Kramers–Kronig relations, as described above.

Comparison of the experimentally extrapolated and simulated refractive indices, allows for interpretation of the origin of the observed P-RSoXS $Q(E)$ variation with energy. We focus our discussion on peak features in the absorptive (β) part of the complex refractive index because those peaks can be directly correlated to specific NEXAFS resonances, while acknowledging that features in the real part (δ), although less directly correlated to NEXAFS resonances, are also significantly responsible for contrast. While the $\pi^*_{C=C}$ (285.25 eV) and σ^*_{C-S} (287 eV) resonances are generally consistent between the two methods, deviations arise at higher energies due to the dominance of σ^*_{C-H} and σ^*_{C-C} features. The σ^*_{C-C} feature dominates in the simulated refractive indices but is less pronounced in the experimental refractive indices. Contrasts calculated from both experimental and simulated refractive indices are shown in Figure 5c,e. Antibonding orbitals above each plot in Figure 5 are labeled based on simulation (Figures S10–S13) and are in agreement with previous assignments for P3HT.[52,58,66,67]

First, we note minimal ISI outside of orientational self-contrast from C 1s → $\pi^*_{C=C}$, σ^*_{C-S}, σ^*_{C-C} transitions, particularly past the absorption edge, which indicates minimal vacuum contrast. Vacuum, when treated as a material with $\beta = 0$ and $\delta = 0$, gives way to binary contrast that is n_i^2 and thus—due to the step edge in β—should give a step edge in contrast past the absorption onset when vacuum contrast is significant. Vacuum contrast may originate in some materials from surface roughness and bulk density fluctuations. Because of the minimal vacuum contrast here, as a first approximation, we will neglect scattering from surface roughness in our simulations.

Second, we note that neither the contrasts calculated from the simulated or experimental refractive indices describe the σ^*_{C-C} feature (centered near 293 eV) in the ISI well. At photon energies higher than 290 eV, contrasts calculated from the experimental refractive indices are minimal. These calculated contrasts do not predict the σ^*_{C-C} feature well, suggesting a greater extent of side chain orientational preference (relative to the extent of conjugated plane orientational preference) in the film bulk than was measured in the experimental NEXAFS spectra. A greater side chain orientational preference combined with overall molecular orientational heterogeneity would then be expected to lead to enhanced scattering contrast across these energies. This interpretation is supported by experimental scattering anisotropy up to 310 eV (see Figure S37), where minimal scattering anisotropy is observed past 292 eV, and by mapping the Lorentz-corrected scattering intensity as a function of q and energy (see Figure S34). The scattering intensity at 293 eV is centered above 0.09 Å^{-1}, offset from the scattering anisotropy centered near 0.04 Å^{-1}, which suggests that this feature is not well-correlated with the fibril length scale, unlike the $\pi^*_{C=C}$ and σ^*_{C-S} resonances. Orientational self-contrasts from the simulated refractive indices appear to better predict the σ^*_{C-C} feature in the ISI because alignment with the ordinary and extraordinary axis is directly simulated and the unit cell exhibits side chains extended from the backbone with a high extent of preferential orientation (shown in Figure 5b). In later sections, we simulate the effect of counterion identity and distribution on P-RSoXS anisotropy using the experimental P3HT
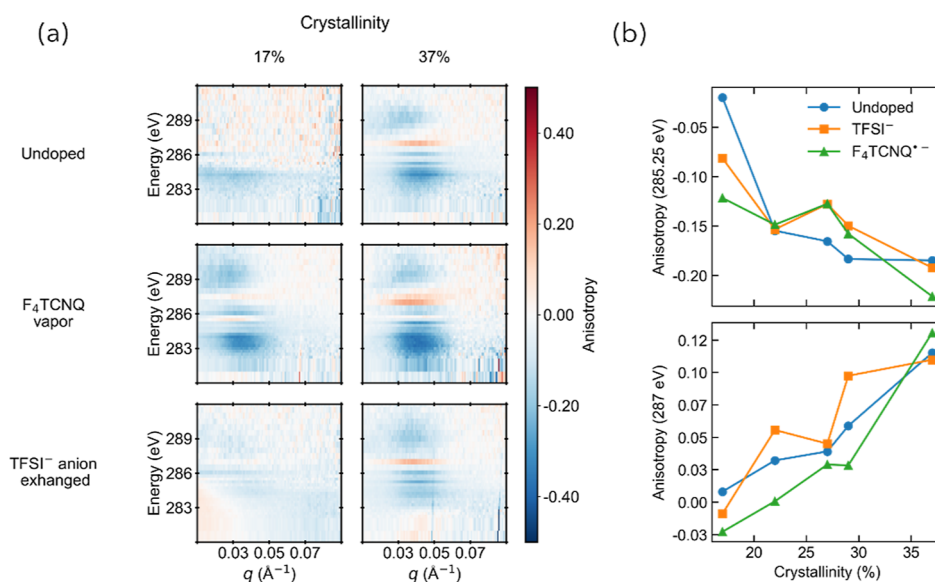
Figure 6. (a) Scattering anisotropy across energies and q as a function of blend compositions and doping. (b) Scattering anisotropy as a function of blend composition and doping at scattering energies of 285.25 eV (top) and 287 eV (bottom), corresponding to the C 1s $\rightarrow \pi^*_{C=C}$ and C 1s $\rightarrow \sigma^*_{C-S}$ transitions, respectively.

refractive indices at the carbon K-edge to facilitate comparisons below 292 eV.

3.5. Experimental Scattering Anisotropy Varies with Crystallinity and Counterion. P-RSoXS data from undoped P3HT films reveals a clear trend: as the degree of crystallinity increases, so does the magnitude of scattering anisotropy up to the C 1s $\rightarrow \sigma^*_{C-S}$ transition at 287 eV, as illustrated in Figure 6. This trend is exemplified by both increased positive scattering anisotropy at the C 1s $\rightarrow \sigma^*_{C-S}$ transition (287 eV), and negative scattering anisotropy at the C 1s $\rightarrow \pi^*_{C=C}$ transition (285.25 eV) and is consistent with what we observe in both samples of greater crystallinity and annealed samples (Figure S35).[34] These observations are in line with predictions of previously established models.[6,34] The shift in the specific value of q where the scattering anisotropy emerges results from either a decrease in the thickness of amorphous regions separating ordered domains or an increase in the proportion of ordered domains themselves. Precise determination of these changes from scattering patterns alone necessitates the analysis of multiple peak orders to distinguish between these possibilities; here, we only observe a single peak across our blend samples.[33] Figure 6 shows scattering anisotropy data for only our least and most crystalline samples; however, a full set of scattering anisotropy data for all blend compositions are available (Figure S36).

In doped films with F$_4$TCNQ$^{\bullet-}$ counterions, the magnitude of (negative) scattering anisotropy at energies less than 283 eV increases across all levels of sample crystallinity, consistent with similar levels of F$_4$TCNQ$^{\bullet-}$ uptake measured across all blends. This enhancement is attributed primarily to F$_4$TCNQ$^{\bullet-}$ having a greater mass density and higher average atomic number composition relative to P3HT, making its β and δ of greater magnitude (either positive or negative) relative to P3HT, a phenomenon we will refer to below as increased optical density. The incorporation of F$_4$TCNQ$^{\bullet-}$ thus makes P3HT more optically dense where F$_4$TCNQ$^{\bullet-}$ is most concentrated. At the N and F K-edges, scattering anisotropy for F$_4$TCNQ-doped samples is observed at the same length scale as the C K-edge scattering across blend composition. The magnitude of

the anisotropy remains relatively constant across compositions (Figures S38 and S39). We note that the fully regiorandom sample shows anisotropy in scattering upon doping due to structural order induced by the chain stiffening by doping as previously observed.[9−11]

When TFSI$^-$ is the counterion in doped films, minimal changes in the magnitude of the scattering anisotropy are observed. TFSI$^-$ lacks a carbon-based π system, in contrast to planar F$_4$TCNQ$^{\bullet-}$, and it has no rigid conformation, resulting in relatively isotropic NEXAFS (simulated TFSI$^-$ NEXAFS are shown in Figures S21 and S31). This isotropy can be seen from a comparison of scattering anisotropy for undoped P3HT and TFSI$^-$-containing doped P3HT in Figure 6, as well as N and F K-edge anisotropy maps, where little to no scattering anisotropy is observed (Figures S38 and S39). Opposite from the F$_4$TCNQ$^{\bullet-}$ case, TFSI$^-$ incorporation leads to a relatively weak inversion in scattering anisotropy at the C K-edge at energies less than 283 eV. We also note that TFSI$^-$ was introduced using an ion-exchange process from films initially doped with F$_4$TCNQ and we may expect only small changes in the overall nanostructure of P3HT, making the comparison of the two cases more robust.

Considering the X-ray refractive indices, it is clear that the optical properties of the dopants will affect the scattering anisotropy due to either a concentration or dilution of optical density in the amorphous/crystalline P3HT domains that these dopants occupy. The difference in optical density between crystalline and amorphous regions is also a source of scattering anisotropy in undoped samples.[35] Selective distributions of dopant to either crystalline or amorphous regions would result in distinct changes to scattering anisotropy. We will exploit this sensitivity to test specific hypotheses related to dopant distribution via P-RSoXS simulation from real-space models.

3.6. Modeling P-RSoXS of Doped Semicrystalline Polymers. To aid in interpreting the doping-induced changes to the experimental scattering anisotropy, we developed a methodology using a digital twin of our model system for P-RSoXS simulations. For this process, we employ the voxel-defined morphology framework of the NIST RSoXS
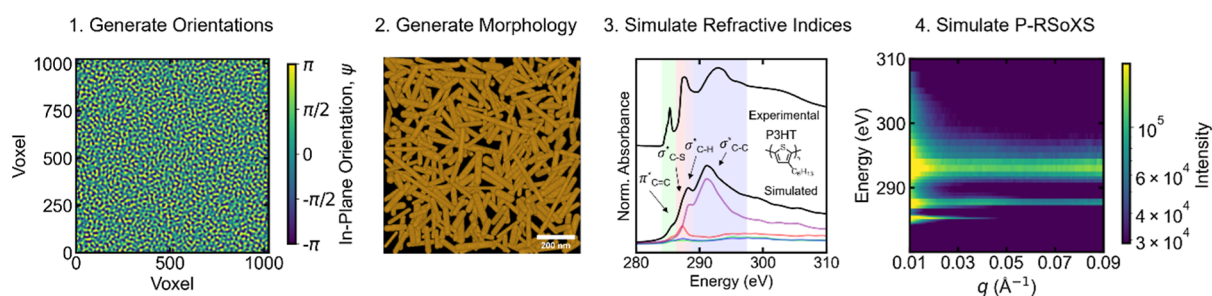
Figure 7. Schematic of the multistep workflow for simulation of RSoXS. First, the generation of orientation fields seeds the simulation space for the orientation of polymer fibrils. Second, a Poisson disk sampling facilitates the random distribution of fibrils with prescribed minimum distances, inheriting orientation during placement. Fibrils grow lengthwise until reaching another fibril or the predefined maximum length. The final morphology distinguishes between fibrillar (crystalline P3HT) and amorphous phases. Third, the orientation of different transition dipoles relative to the X-ray polarization are used to calculate the effective optical properties for each voxel. The combined morphology and refractive indices are used as inputs to the simulation of RSoXS patterns.
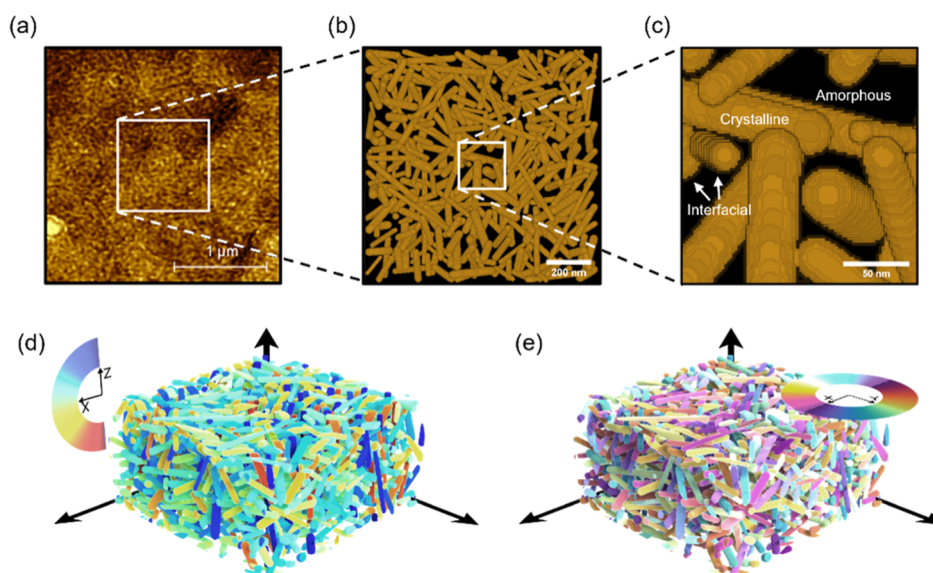
Figure 8. (a) Atomic force microscopy phase contrast image showing fibrillar crystallites of P3HT. (b) Simulated P3HT morphology, comparable in area to the region highlighted in (a). (c) Magnified inset of the simulated morphology, showing individual voxels composing crystalline, amorphous, and interfacial domains. (d) Simulated morphology with fibrils colored to indicate out-of-plane angle, θ. (e) The same simulated morphology as in (d), recolored to denote fibril in-plane angle, ψ.

Simulation Suite (NRSS) in the four-step workflow as outlined in Figure 7.[32]

We initiated the simulation by defining a box and voxel pitch that represent the P-RSoXS experimental length scales, specifically within a q-range of 0.01–0.1 Å^{-1} corresponding to periodicities from 63 to 6.3 nm. Orientation fields were employed to seed fibrils and ensure in-plane isotropy (random ψ, see Figure 8e) and orientation with respect to the substrate normal (θ, see Figure 8d) as inferred from GIWAXS data (see Figures S7–S9). The orientation fields were Gaussian Random Fields (GRFs) generated using a power spectral density and normalized with a cumulative distribution function. Figure S9 demonstrates the simulated scattering anisotropy versus edge-on character, highlighting minor variances between the least and most edge-on aligned samples and minimal changes to edge-on character upon doping. Thus, the average orientation distribution across all samples was used to isolate the effect of the distribution and identity of the counterion. Within the defined simulation box, voxelized fibrils were introduced sequentially. These fibrils possess a Gaussian distribution of diameters (15 nm ± 3 nm) and an initial length of 100 nm,

growing lengthwise until they either achieve a maximum length of 400 nm or encounter another fibril. Voxels within the fibrillar areas are classified as crystalline, with the C 1s → $\pi^*_{C=C}$ extraordinary index of alignment parallel to the fibril long axis.[58] The surrounding matrix is identified as amorphous with 10% less density than crystalline P3HT and exhibits isotropic P3HT optical properties.[35] A Gaussian filter with a standard deviation of 3 was employed at the crystalline–amorphous boundary to define interfacial width. Figure 8 presents a rendered, illustrative example of the simulated morphology, providing a comparison with fibril texture measured by AFM.

For dopant incorporation, we replaced certain fractions of P3HT volume with the dopant placed either uniformly, within crystallites, or within amorphous regions. The total dopant concentration was normalized to concentrations determined from XPS measurements, shown above. The orientation of TFSI$^-$ and F$_4$TCNQ$^{\bullet-}$ is randomized in isotropic models. We also considered multiple alignment models for F$_4$TCNQ$^{\bullet-}$ within P3HT crystals: a coaligned model where F$_4$TCNQ$^{\bullet-}$ shares orientation with P3HT (parallel C 1s → $\pi^*_{C=C}$

transition dipole moments), and antialigned $F_4TCNQ^{\bullet-}$ by rotating the coaligned extraordinary axis 90° about the intrinsic *X*-axis. This geometry places the $F_4TCNQ^{\bullet-}$ C 1s → $\pi^*_{C=C}$ transition dipole moment parallel to the conjugated plane of P3HT. A subsequent random rotation about the intrinsic *Y*-axis enables a random distribution of $F_4TCNQ^{\bullet-}$ C 1s → $\pi^*_{C=C}$ transition dipole moments within the P3HT conjugated plane. Finally, the net refractive indices of each simulated voxel represent the volume-fraction weighted sum of individual material refractive indices. For P3HT, experimentally extrapolated refractive indices are used for all P-RSoXS simulations at the carbon K-edge. For the N and F K-edges, the refractive indices of P3HT are calculated from atomic scattering factors considering density (1.1 g/cm³) and stoichiometry. For TFSI⁻ and $F_4TCNQ^{\bullet-}$ counterions across the C, N, and F K-edges, simulated refractive indices are used.

3.7. Simulation-Aided Interpretation of P-RSoXS Scattering Anisotropy.
We use the model developed above to test the hypothetical scenarios for the dopant distribution illustrated in Figure 1: a uniform distribution across the polymer, localization within crystallites, and localization within amorphous regions. In each scenario, we maintained a consistent doping level, ensuring that the total dopant volume fraction remains equivalent across all distributions by proportionately replacing the material in a specified phase (crystalline, amorphous, or uniform) with dopant. We focus on the highest-crystallinity sample here and show the results for other fractions in the Supporting Information. We examined the case of TFSI⁻ to probe the effect of dopant distribution alone, given its relatively isotropic X-ray optical constants at the C K-edge (Figure S31). The effect of dopant orientation was examined using P3HT and $F_4TCNQ^{\bullet-}$ by modeling three distinct relative alignments of the C 1s → $\pi^*_{C=C}$ transition dipole moments: isotropic, coaligned, and antialigned. It is important to note that these orientations are defined with respect to the crystalline P3HT, ensuring that the orientation of F_4TCNQ is consistently measured against the P3HT C 1s → $\pi^*_{C=C}$ transition dipole moments. We find that at the F_4TCNQ concentrations observed (<2.5 mol % $F_4TCNQ/F_4TCNQ^{\bullet-}$ relative to P3HT repeat units), the scattering anisotropy at the C K-edge does not sufficiently distinguish between the three cases for the orientation. We note that the simulated fibrils, based on random orientation fields, do not perfectly capture the peak feature locations. Despite these limitations, our simulations distinctly delineate the effects of various dopant distributions and help interpret the observed anisotropies. The role of varying dopant concentration and polymer density was examined by scaling their optical densities by ±20% and simulating the resultant scattering anisotropies (see Figures S49−S60); within this variation, the features in the simulated scattering anisotropy are consistent.

In Figure 9, we show the models (based on 35% crystalline simulated morphologies) that are most consistent with the experimentally observed scattering anisotropy for 37% crystalline P3HT containing $F_4TCNQ^{\bullet-}$ and TFSI⁻ counterions. The experimental scattering anisotropy at the C K-edge across all blends (from 17% to 37% crystallinity) is shown in Figure S36. We first consider the changes to scattering anisotropy arising from varying dopant distributions. For TFSI⁻, which exhibits relatively isotropic optical properties, the primary effect of differing distributions—whether uniform across the polymer, localized within crystallites, or localized
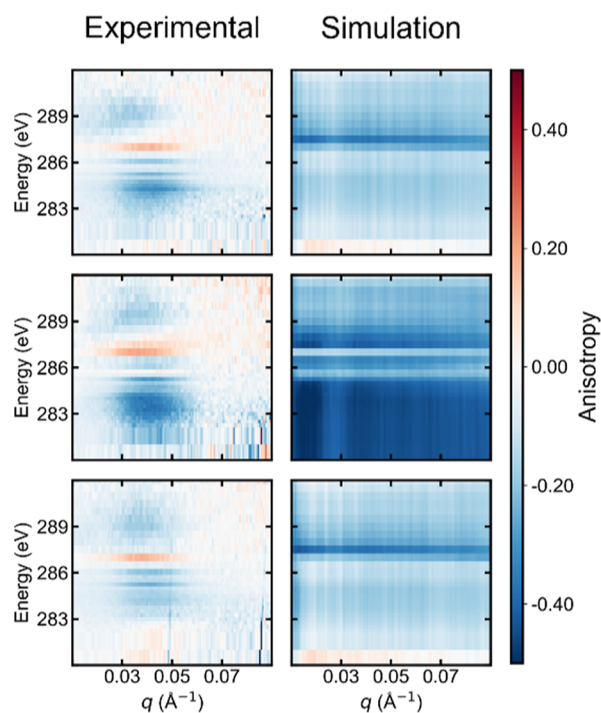
Figure 9. Comparison of experimental scattering anisotropy in 37% crystalline P3HT films (left) and simulated scattering anisotropy in 35% crystalline P3HT films (right). The experimental cases (left) show undoped P3HT (top), F_4TCNQ-doped P3HT (center), and TFSI⁻-anion exchanged, doped P3HT (bottom). The simulated cases (right) correspond to undoped P3HT (top), F_4TCNQ^- counterions localized within crystallites and oriented perpendicular to the polymer backbone (center), and uniformly distributed, randomly oriented TFSI⁻ counterions (bottom).

within amorphous regions—is a modulation of the effective optical density in these areas. Differences in density contrast between crystalline and amorphous P3HT have previously been assigned to account for scattering anisotropy.[35] Given that TFSI⁻ exhibits roughly half the optical density of P3HT at the C K-edge (see Figures S24 and S31 for P3HT and TFSI⁻ refractive indices, respectively), the replacement of P3HT with TFSI⁻ effectively diminishes the optical density of the voxel in the model. Localized TFSI⁻ within amorphous domains leads to a pronounced positive scattering anisotropy below 283 eV; in contrast, if TFSI⁻ is confined to the crystallites a negative scattering anisotropy at sub-283 eV energies results (Figure S40). Uniform doping negligibly impacts the scattering anisotropy, which is still dominated by P3HT itself. While simulations alone do not confirm a uniform distribution of TFSI⁻, the experimental observations shown in Figure 6 correlate best with a uniform distribution model of TFSI⁻. A relatively uniform distribution of TFSI⁻ is also reasonable given our observation of a higher doping level from the ion exchange process (Figure 3).

In the case of isotropic, randomly oriented $F_4TCNQ^{\bullet-}$, which exhibits β and δ approximately 4× that of P3HT, a reversed trend is observed: negative scattering anisotropy below 283 eV when it is localized within crystallites and an inversion when $F_4TCNQ^{\bullet-}$ is within amorphous regions. The simulated variations in the scattering anisotropy for isotropic dopants highlight that the direction and magnitude of scattering anisotropy can distinctly differentiate between
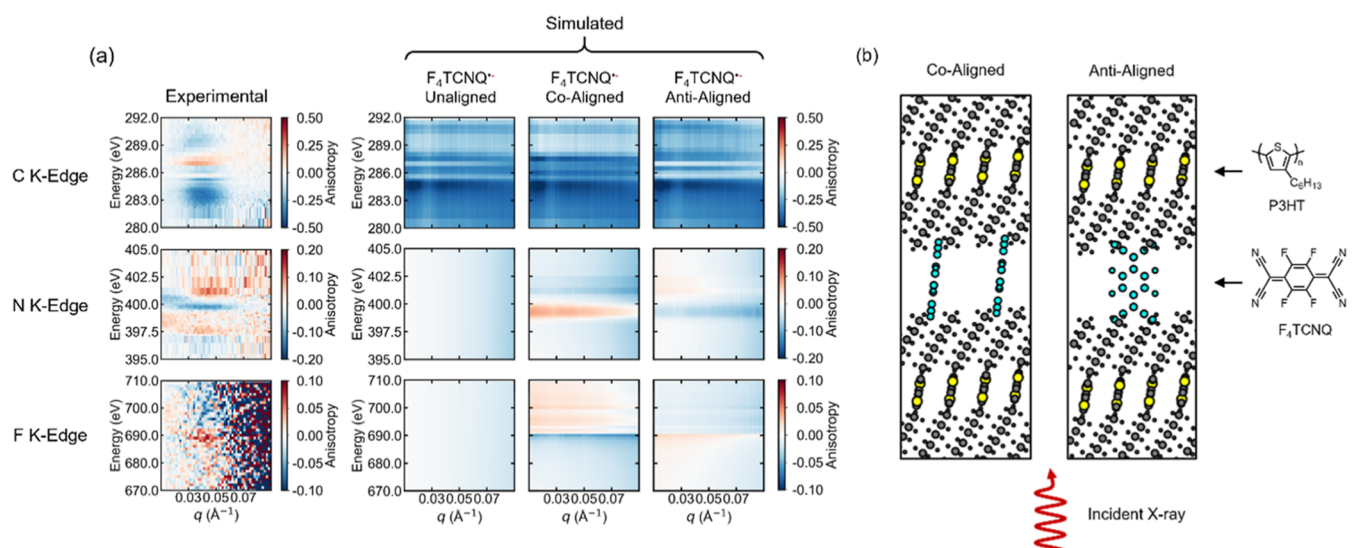
Figure 10. (a) Comparison of experimental and simulated scattering anisotropy in 37% crystalline P3HT films with varying orientations of F$_4$TCNQ$^{\bullet-}$ relative to P3HT. Experimental scattering anisotropy maps at the C, N, F K-edges shown next to simulated scattering anisotropy maps for unaligned, parallel, and perpendicular F$_4$TCNQ$^{\bullet-}$ relative to P3HT. (b) Schematic representations of the simulated relative alignments of F$_4$TCNQ$^{\bullet-}$ to P3HT in ordered domains and the direction of propagation of the incident X-ray for P3HT domain that is edge-on with respect to the substrate.

dopant distributions due to the influence of changing optical densities in different phases.

We also examined the influence of the orientation of the F$_4$TCNQ$^{\bullet-}$ counterion on the simulated scattering anisotropy. We modeled specific relative orientations of F$_4$TCNQ$^{\bullet-}$ within the P3HT crystallites that we refer to as unaligned, coaligned, and antialigned configurations (refer to Figure 10 for visualization). Our C K-edge simulations indicate that the scattering anisotropy patterns of these orientations are not sufficiently distinct to determine the orientation of F$_4$TCNQ$^{\bullet-}$ within semicrystalline films. This result suggests that at the C K-edge, the scattering anisotropy is predominantly influenced by variations in optical density rather than the orientation of F$_4$TCNQ$^{\bullet-}$. However, at the N and F K-edges—where P3HT does not absorb and the contribution of F$_4$TCNQ$^{\bullet-}$ more pronounced—we observe clearer evidence of preferential orientation. Particularly at the N K-edge, both experimental and simulated data of perpendicular configurations reveal a transition from more positive to negative to positive scattering anisotropy with increasing energy from near 399 to 401 eV, indicative of a predominant anti-aligned orientation of F$_4$TCNQ$^{\bullet-}$ within the crystallites, as illustrated in Figure 10b. The experimental pattern at the F K-edge is less distinct at low scattering vectors with smaller scattering anisotropy than the other edges, but the crossover in sign near q = 0.04 Å^{-1} is consistent with the simulation of the antialigned orientation. This structure is also consistent with studies of the relative orientation of the backbone of P3HT and F$_4$TCNQ$^{\bullet-}$ observed by polarized optical absorption in oriented films.[68] Overall the experiments and simulations support that it is possible to discern the relative molecular orientation of the counterion and conjugated polymer backbone in the ordered domains of a semicrystalline polymer film.

We note that across varying blend compositions, F$_4$TCNQ-doped blends exhibit scattering anisotropy with relatively consistent sign and magnitude (see Figures S36−S39), across the C, N, and F K-edges. This observation is in contrast to the

undoped blends where the scattering anisotropy maxima and fluctuations in intensity scale with the composition of the blend (see Figure 6). Our simulations of morphologies with lower crystalline volume fractions also show that scattering anisotropy at the C K-edge, driven by differences in density between ordered and disordered P3HT domains, scales with crystallinity (see Figures S40−S42). Interestingly, simulations of these lower crystallinity morphologies at the N and F K-edges exhibit increased scattering anisotropy (see Figures S43−S48). The consistency in the magnitude of the scattering anisotropy across all elemental edges is consistent with doping-induced ordering of P3HT.[9−11]

In conclusion, our findings illustrate that for P3HT and the counterions considered here, the orientational self-contrast at the C K-edge is less significant than the effect of the changing optical density, which presents a challenge in resolving both aspects using a single elemental edge. However, by focusing on the unique orientational contrast at the N and F K-edges for F$_4$TCNQ$^{\bullet-}$, we successfully isolated and discernedits orientation relative to ordered chains of P3HT. This insight not only advances our comprehension of scattering anisotropy but also underscores the intricate interplay between the distribution of counterions and their relative orientation in ordered domains, and the resultant X-ray optical properties in doped conjugated polymers.

4. CONCLUSIONS

To understand the distribution of counterions within the crystalline and amorphous phases of doped P3HT, we examined a range of P3HT blends, to control crystallinity, and incorporated chemically distinct counterions. Our investigation utilized P-RSoXS to probe the nanostructure, compositional, and orientational distributions in doped P3HT blends. To isolate the effect of the identity and the distribution of the counterions, we complemented P-RSoXS with experimental techniques to define the composition and the distribution of orientations of ordered fibrils. The two counterions examined here had differing soft X-ray absorption

spectra and anisotropies due to their structure, with TFSI⁻ being relatively isotropic and F₄TCNQ•⁻ being planar. Our findings reveal that the inherent scattering anisotropy of P3HT, driven by the orientational self-contrast and differences in optical density between the crystalline and amorphous regions, can be modified by the spatial distribution of counterions. We find that the scattering anisotropy is not strongly modified with TFSI⁻ incorporation despite its lower optical density at the C K-edge. The simulation with uniform distribution of TFSI⁻ is consistent with the experiment, but the small change in anisotropy prevents a definitive assessment of the distribution. Conversely, F₄TCNQ increases the scattering anisotropy through its incorporation within crystallites. By leveraging the anisotropic refractive indices of F₄TCNQ at the N and F K-edges, we find that its conjugated plane is oriented perpendicularly to that of P3HT in crystalline domains. Our results show that P-RSoXS can reveal orientations of multiple chemical species in doped semicrystalline polymers.

This specific case demonstrates a workflow for creating morphological models and integrating orientation-dependent refractive indices into P-RSoXS simulations, crucial for understanding the complex effects of orientation, composition, and structure. This methodology not only highlights the unique compositional and orientational sensitivities of P-RSoXS but also helps paves the way for future workflows to capitalize on its unique insights to develop structure−property relationships across soft matter systems and to leverage advances in computational analysis of 2D scattering patterns.[69] For example, we anticipate the methodology will be useful in systems such as salt-doped polymers for electrolytes,[70−72] membranes for separations,[73,74] blends for organic photo-voltaics,[63,75,76] and organic electrochemical transistors.[77]

ASSOCIATED CONTENT

Data Availability Statement

Data Availability: Data is available free of charge from the Dryad repository at DOI: 10.5061/dryad.6t1g1jx65.

Ⓢ Supporting Information

The Supporting Information is available free of charge at https://pubs.acs.org/doi/10.1021/acs.jpcb.4c05774.

> Summary of P3HT blend compositions, crystallinity, and dopant/counterion mole fractions of P3HT blends, atomic force microscopy images of doped and undoped P3HT blend films, X-ray photoelectron spectroscopy (XPS) depth profiles of doped P3HT films, details on absorbance correction for scattered intensity, grazing incidence wide angle X-ray scattering (GIWAXS) analysis of P3HT aggregate orientation, comparisons of simulated and experimentally measured near-edge X-ray absorbance fine structure (NEXAFS) spectra, exper-imental and simulated scattering anisotropy as function blend composition and doping for C, N, and F K-edges (PDF)

AUTHOR INFORMATION

Corresponding Authors

Dean M. DeLongchamp − *Materials Measurement Laboratory, National Institute of Standards and Technology, Gaithersburg, Maryland 20899, United States;* Ⓞ orcid.org/0000-0003-0840-0757; Email: dean.delongchamp@nist.gov

Michael L. Chabinyc − *Materials Department, University of California at Santa Barbara, Santa Barbara, California 93117, United States;* Ⓞ orcid.org/0000-0003-4641-3508; Email: mchabinyc@engineering.ucsb.edu

Authors

Phong H. Nguyen − *Department of Chemical Engineering, University of California at Santa Barbara, Santa Barbara, California 93117, United States*

Devon Callan − *Department of Chemical Engineering, University of California at Santa Barbara, Santa Barbara, California 93117, United States*

Evan Plunkett − *Materials Department, University of California at Santa Barbara, Santa Barbara, California 93117, United States*

Max Gruschka − *Department of Chemistry and Biochemistry, University of California at Santa Barbara, Santa Barbara, California 93117, United States*

Nima Alizadeh − *Materials Department, University of California at Santa Barbara, Santa Barbara, California 93117, United States*

Matthew R. Landsman − *Advanced Light Source, Lawrence Berkeley National Laboratory, Berkeley, California 94720, United States; Department of Civil, Architectural, and Environmental Engineering, University of Texas at Austin, Austin, Texas 78712, United States*

Gregory M. Su − *Advanced Light Source, Lawrence Berkeley National Laboratory, Berkeley, California 94720, United States; Materials Sciences Division, Lawrence Berkeley National Laboratory, Berkeley, California 92720, United States;* Ⓞ orcid.org/0000-0001-7495-8041

Eliot Gann − *National Synchrotron Light Source II, Brookhaven National Laboratory, Upton, New York 11973, United States*

Christopher M. Bates − *Department of Chemical Engineering, University of California at Santa Barbara, Santa Barbara, California 93117, United States; Materials Department and Department of Chemistry and Biochemistry, University of California at Santa Barbara, Santa Barbara, California 93117, United States;* Ⓞ orcid.org/0000-0002-1598-794X

Complete contact information is available at:
https://pubs.acs.org/10.1021/acs.jpcb.4c05774

Notes

The authors declare no competing financial interest.

ACKNOWLEDGMENTS

■ REFERENCES

(1) Scaccabarozzi, A. D.; Basu, A.; Aniés, F.; Liu, J.; Zapata-Arteaga, O.; Warren, R.; Firdaus, Y.; Nugraha, M. I.; Lin, Y.; Campoy-Quiles, M.; et al. Doping Approaches for Organic Semiconductors. *Chem. Rev.* **2022**, *122* (4), 4420−4492.

(2) Thomas, E. M.; Nguyen, P. H.; Jones, S. D.; Chabinyc, M. L.; Segalman, R. A. Electronic, Ionic, and Mixed Conduction in Polymeric Systems. *Annu. Rev. Mater. Res.* **2021**, *51* (1), 1−20.

(3) Thomas, E. M.; Peterson, K. A.; Balzer, A. H.; Rawlings, D.; Stingelin, N.; Segalman, R. A.; Chabinyc, M. L. Effects of Counter-Ion Size on Delocalization of Carriers and Stability of Doped Semiconducting Polymers. *Adv. Electron. Mater.* **2020**, *6* (12), 2000595.

(4) Jacobs, I. E.; D'Avino, G.; Lemaur, V.; Lin, Y.; Huang, Y.; Chen, C.; Harrelson, T. F.; Wood, W.; Spalek, L. J.; Mustafa, T.; et al. Structural and Dynamic Disorder, Not Ionic Trapping, Controls Charge Transport in Highly Doped Conducting Polymers. *J. Am. Chem. Soc.* **2022**, *144* (7), 3005−3019.

(5) Arkhipov, V. I.; Heremans, P.; Emelianova, E. V.; Bässler, H. Effect of Doping on the Density-of-States Distribution and Carrier Hopping in Disordered Organic Semiconductors. *Phys. Rev. B* **2005**, *71* (4), 045214.

(6) Litofsky, J. H.; Lee, Y.; Aplan, M. P.; Kuei, B.; Hexemer, A.; Wang, C.; Wang, Q.; Gomez, E. D. Polarized Soft X-Ray Scattering Reveals Chain Orientation within Nanoscale Polymer Domains. *Macromolecules* **2019**, *52* (7), 2803−2813.

(7) Kohn, P.; Rong, Z.; Scherer, K. H.; Sepe, A.; Sommer, M.; Müller-Buschbaum, P.; Friend, R. H.; Steiner, U.; Hüttner, S. Crystallization-Induced 10-Nm Structure Formation in P3HT/PCBM Blends. *Macromolecules* **2013**, *46* (10), 4002−4013.

(8) McNeill, C. R. Resonant Tender X-Ray Scattering of Organic Semiconductors. *Acc. Mater. Res.* **2023**, *4* (1), 16−26.

(9) Lim, E.; Glaudell, A. M.; Miller, R.; Chabinyc, M. L. The Role of Ordering on the Thermoelectric Properties of Blends of Regioregular and Regiorandom Poly(3-Hexylthiophene). *Adv. Electron. Mater.* **2019**, *5* (11), 1800915.

(10) Liu, W.; Müller, L.; Ma, S.; Barlow, S.; Marder, S. R.; Kowalsky, W.; Köhn, A.; Lovrincic, R. Origin of the π−π Spacing Change upon Doping of Semiconducting Polymers. *J. Phys. Chem. C* **2018**, *122* (49), 27983−27990.

(11) Yee, P. Y.; Scholes, D. T.; Schwartz, B. J.; Tolbert, S. H. Dopant-Induced Ordering of Amorphous Regions in Regiorandom P3HT. *J. Phys. Chem. Lett.* **2019**, *10* (17), 4929−4934.

(12) Watts, K. E.; Neelamraju, B.; Ratcliff, E. L.; Pemberton, J. E. Stability of Charge Transfer States in F4TCNQ-Doped P3HT. *Chem. Mater.* **2019**, *31* (17), 6986−6994.

(13) Neelamraju, B.; Watts, K. E.; Pemberton, J. E.; Ratcliff, E. L. Correlation of Coexistent Charge Transfer States in F4TCNQ-Doped P3HT with Microstructure. *J. Phys. Chem. Lett.* **2018**, *9* (23), 6871−6877.

(14) Wu, E. C.-K.; Salamat, C. Z.; Tolbert, S. H.; Schwartz, B. J. Molecular Dynamics Study of the Thermodynamics of Integer Charge Transfer vs Charge-Transfer Complex Formation in Doped Conjugated Polymers. *ACS Appl. Mater. Interfaces* **2022**, *14*, 26988−27001.

(15) Thomas, E. M.; Brady, M. A.; Nakayama, H.; Popere, B. C.; Segalman, R. A.; Chabinyc, M. L. X-Ray Scattering Reveals Ion-Induced Microstructural Changes During Electrochemical Gating of Poly(3-Hexylthiophene). *Adv. Funct. Mater.* **2018**, *28*, 1803687.

(16) Untilova, V.; Zeng, H.; Durand, P.; Herrmann, L.; Leclerc, N.; Brinkmann, M. Intercalation and Ordering of F6TCNNQ and F4TCNQ Dopants in Regioregular Poly(3-Hexylthiophene) Crystals: Impact on Anisotropic Thermoelectric Properties of Oriented Thin Films. *Macromolecules* **2021**, *54* (13), 6073−6084.

(17) Giridharagopal, R.; Flagg, L. Q.; Harrison, J. S.; Ziffer, M. E.; Onorato, J.; Luscombe, C. K.; Ginger, D. S. Electrochemical Strain Microscopy Probes Morphology-Induced Variations in Ion Uptake and Performance in Organic Electrochemical Transistors. *Nat. Mater.* **2017**, *16* (7), 737−742.

(18) Flagg, L. Q.; Onorato, J. W.; Luscombe, C. K.; Bhat, V.; Risko, C.; Levy-Wendt, B.; Toney, M. F.; McNeill, C. R.; Freychet, G.; Zhernenkov, M.; et al. Resonant X-Ray Diffraction Reveals the Location of Counterions in Doped Organic Mixed Ionic Conductors. *Chem. Mater.* **2023**, *35* (10), 3960−3967.

(19) Jackson, S. R.; Kingsford, R. L.; Collins, G. W.; Bischak, C. G. Crystallinity Determines Ion Injection Kinetics and Local Ion Density in Organic Mixed Conductors. *Chem. Mater.* **2023**, *35*, 5392−5400.

(20) Scholes, D. T.; Yee, P. Y.; Lindemuth, J. R.; Kang, H.; Onorato, J.; Ghosh, R.; Luscombe, C. K.; Spano, F. C.; Tolbert, S. H.; Schwartz, B. J. The Effects of Crystallinity on Charge Transport and the Structure of Sequentially Processed F4TCNQ-Doped Conjugated Polymer Films. *Adv. Funct. Mater.* **2017**, *27* (44), 1702654.

(21) Duong, D. T.; Wang, C.; Antono, E.; Toney, M. F.; Salleo, A. The Chemical and Structural Origin of Efficient P-Type Doping in P3HT. *Org. Elec.* **2013**, *14* (5), 1330−1336.

(22) Gao, J.; Niles, E. T.; Grey, J. K. Aggregates Promote Efficient Charge Transfer Doping of Poly(3-Hexylthiophene). *J. Phys. Chem. Lett.* **2013**, *4* (17), 2953−2957.

(23) Harris, J. K.; Neelamraju, B.; Ratcliff, E. L. Intersystem Subpopulation Charge Transfer and Conformational Relaxation Preceding in Situ Conductivity in Electrochemically Doped Poly(3-Hexylthiophene) Electrodes. *Chem. Mater.* **2019**, *31* (17), 6870−6879.

(24) Cochran, J. E.; Junk, M. J. N.; Glaudell, A. M.; Miller, P. L.; Cowart, J. S.; Toney, M. F.; Hawker, C. J.; Chmelka, B. F.; Chabinyc, M. L. Molecular Interactions and Ordering in Electrically Doped Polymers: Blends of PBTTT and F4TCNQ. *Macromolecules* **2014**, *47* (19), 6836−6846.

(25) Jacobs, I. E.; Lin, Y.; Huang, Y.; Ren, X.; Simatos, D.; Chen, C.; Tjhe, D.; Statz, M.; Lai, L.; Finn, P. A.; Neal, W. G.; et al. High-Efficiency Ion-Exchange Doping of Conducting Polymers. *Adv. Mater.* **2022**, *34* (22), 2102988.

(26) Thomas, E. M.; Davidson, E. C.; Katsumata, R.; Segalman, R. A.; Chabinyc, M. L. Branched Side Chains Govern Counterion Position and Doping Mechanism in Conjugated Polythiophenes. *ACS Macro Lett.* **2018**, *7* (12), 1492−1497.

(27) Untilova, V.; Biskup, T.; Biniek, L.; Vijayakumar, V.; Brinkmann, M. Control of Chain Alignment and Crystallization Helps Enhance Charge Conductivities and Thermoelectric Power Factors in Sequentially Doped P3HT:F4TCNQ Films. *Macromolecules* **2020**, *53* (7), 2441–2453.

(28) Zhong, Y.; Untilova, V.; Muller, D.; Guchait, S.; Kiefer, C.; Herrmann, L.; Zimmermann, N.; Brosset, M.; Heiser, T.; Brinkmann, M. Preferential Location of Dopants in the Amorphous Phase of Oriented Regioregular Poly(3-Hexylthiophene-2,5-Diyl) Films Helps Reach Charge Conductivities of 3000 S Cm−1. *Adv. Funct. Mater.* **2022**, *32* (30), 2202075.

(29) Hynynen, J.; Kiefer, D.; Müller, C. Influence of Crystallinity on the Thermoelectric Power Factor of P3HT Vapour-Doped with F4TCNQ. *RSC Adv.* **2018**, *8* (3), 1593–1599.

(30) Collins, B. A.; Gann, E. Resonant Soft X-Ray Scattering in Polymer Science. *J. Polym. Sci.* **2022**, *60* (7), 1199–1243.

(31) Freychet, G.; Chantler, P.; Huang, Y.; Tan, W. L.; Zhernenkov, M.; Nayak, N.; Kumar, A.; Gilhooly-Finn, P. A.; Nielsen, C. B.; Thomsen, L.; et al. Resolving the Backbone Tilt of Crystalline Poly(3-Hexylthiophene) with Resonant Tender X-Ray Diffraction. *Mater. Horiz.* **2022**, *9* (6), 1649–1657.

(32) Saurabh, K.; Dudenas, P. J.; Gann, E.; Reynolds, V. G.; Mukherjee, S.; Sunday, D.; Martin, T. B.; Beaucage, P. A.; Chabinyc, M. L.; DeLongchamp, D. M.; et al. CyRSoXS: A GPU-Accelerated Virtual Instrument for Polarized Resonant Soft X-Ray Scattering. *J. Appl. Crystallogr.* **2023**, *56* (3), 868–883.

(33) Reynolds, V. G.; Callan, D. H.; Saurabh, K.; Murphy, E. A.; Albanese, K. R.; Chen, Y.-Q.; Wu, C.; Gann, E.; Hawker, C. J.; Ganapathysubramanian, B.; et al. Simulation-Guided Analysis of Resonant Soft X-Ray Scattering for Determining the Microstructure of Triblock Copolymers. *Mol. Syst. Des. Eng.* **2022**, *7* (11), 1449–1458.

(34) Litofsky, J. H.; Gomez, E. D. Connecting Soft X-Ray Anisotropy with Local Order in Conjugated Polymers. *MRS Commun.* **2019**, *9* (4), 1168–1173.

(35) Mukherjee, S.; Gann, E.; Nahid, M. M.; McAfee, T.; Herzing, A. A.; DeLongchamp, D. M.; Ade, H. Orientational Ordering within Semiconducting Polymer Fibrils. *Adv. Funct. Mater.* **2021**, *31* (28), 2102522.

(36) Lim, E.; Peterson, K. A.; Su, G. M.; Chabinyc, M. L. Thermoelectric Properties of Poly(3-Hexylthiophene) (P3HT) Doped with 2,3,5,6-Tetrafluoro-7,7,8,8-Tetracyanoquinodimethane (F4TCNQ) by Vapor-Phase Infiltration. *Chem. Mater.* **2018**, *30* (3), 998–1010.

(37) Clark, J.; Chang, J.-F.; Spano, F. C.; Friend, R. H.; Silva, C. Determining Exciton Bandwidth and Film Microstructure in Polythiophene Films Using Linear Absorption Spectroscopy. *Appl. Phys. Lett.* **2009**, *94* (16), 163306.

(38) Spano, F. C. Modeling Disorder in Polymer Aggregates: The Optical Spectroscopy of Regioregular Poly (3-Hexylthiophene) Thin Films. *J. Chem. Phys.* **2005**, *122* (23), 234701.

(39) Spano, F. C. Absorption in Regio-Regular Poly(3-Hexyl)-Thiophene Thin Films: Fermi Resonances, Interband Coupling and Disorder. *Chem. Phys.* **2006**, *325* (1), 22–35.

(40) Ilavsky, J. Nika: Software for Two-Dimensional Data Reduction. *J. Appl. Crystallogr.* **2012**, *45* (2), 324–328.

(41) Gann, E.; Crofts, T.; Holland, G.; Beaucage, P.; McAfee, T.; Kline, R. J.; Collins, B. A.; McNeill, C. R.; Fischer, D. A.; DeLongchamp, D. M. A NIST Facility for Resonant Soft X-Ray Scattering Measuring Nano-Scale Soft Matter Structure at NSLS-II. *J. Phys.: Condens. Matter* **2021**, *33* (16), 164001.

(42) Kieffer, J.; Valls, V.; Blanc, N.; Hennig, C. New Tools for Calibrating Diffraction Setups. *J. Synchrotron. Rad.* **2020**, *27* (2), 558–566.

(43) Bunău, O.; Calandra, M. Projector Augmented Wave Calculation of X-Ray Absorption Spectra at the $L_{2,3}$ Edges. *Phys. Rev. B* **2013**, *87* (20), 205105.

(44) Gougoussis, C.; Calandra, M.; Seitsonen, A. P.; Mauri, F. First-Principles Calculations of x-Ray Absorption in a Scheme Based on

Ultrasoft Pseudopotentials: From α-Quartz to High-T$_c$ Compounds. *Phys. Rev. B* **2009**, *80* (7), 075102.

(45) Taillefumier, M.; Cabaret, D.; Flank, A.-M.; Mauri, F. X-Ray Absorption near-Edge Structure Calculations with the Pseudopotentials: Application to the K Edge in Diamond and α-Quartz. *Phys. Rev. B* **2002**, *66* (19), 195107.

(46) Giannozzi, P.; Baroni, S.; Bonini, N.; Calandra, M.; Car, R.; Cavazzoni, C.; Ceresoli, D.; Chiarotti, G. L.; Cococcioni, M.; Dabo, I.; et al. QUANTUM ESPRESSO: A Modular and Open-Source Software Project for Quantum Simulations of Materials. *J. Phys.: Condens. Matter* **2009**, *21* (39), 395502.

(47) Giannozzi, P.; Andreussi, O.; Brumme, T.; Bunau, O.; Buongiorno Nardelli, M.; Calandra, M.; Car, R.; Cavazzoni, C.; Ceresoli, D.; Cococcioni, M.; et al. Advanced Capabilities for Materials Modelling with Quantum ESPRESSO. *J. Phys.: Condens. Matter* **2017**, *29* (46), 465901.

(48) Zhugayevych, A.; Mazaleva, O.; Naumov, A.; Tretiak, S. Lowest-Energy Crystalline Polymorphs of P3HT. *J. Phys. Chem. C* **2018**, *122* (16), 9141–9151.

(49) Watts, B. Calculation of the Kramers-Kronig Transform of X-Ray Spectra by a Piecewise Laurent Polynomial Method. *Opt. Express* **2014**, *22* (19), 23628–23639.

(50) Gann, E.; McNeill, C. R.; Tadich, A.; Cowie, B. C. C.; Thomsen, L. Quick AS NEXAFS Tool (QANT): A Program for NEXAFS Loading and Analysis Developed at the Australian Synchrotron. *J. Synchrotron Rad.* **2016**, *23* (1), 374–380.

(51) Dudenko, D.; Kiersnowski, A.; Shu, J.; Pisula, W.; Sebastiani, D.; Spiess, H. W.; Hansen, M. R. A Strategy for Revealing the Packing in Semicrystalline π-Conjugated Polymers: Crystal Structure of Bulk Poly-3-Hexyl-Thiophene (P3HT). *Angew. Chem. Int. Ed.* **2012**, *51* (44), 11068–11072.

(52) Su, G. M.; Patel, S. N.; Pemmaraju, C. D.; Prendergast, D.; Chabinyc, M. L. First-Principles Predictions of Near-Edge X-Ray Absorption Fine Structure Spectra of Semiconducting Polymers. *J. Phys. Chem. C* **2017**, *121* (17), 9142–9152.

(53) Ko, S.; Hoke, E. T.; Pandey, L.; Hong, S.; Mondal, R.; Risko, C.; Yi, Y.; Noriega, R.; McGehee, M. D.; Brédas, J. L.; et al. Controlled Conjugated Backbone Twisting for an Increased Open-Circuit Voltage While Having a High Short-Circuit Current in Poly(Hexylthiophene) Derivatives. *J. Am. Chem. Soc.* **2012**, *134* (11), 5222–5232.

(54) McCulloch, B.; Ho, V.; Hoarfrost, M.; Stanley, C.; Do, C.; Heller, W. T.; Segalman, R. A. Polymer Chain Shape of Poly(3-Alkylthiophenes) in Solution Using Small-Angle Neutron Scattering. *Macromolecules* **2013**, *46* (5), 1899–1907.

(55) Nagai, M.; Huang, J.; Zhou, T.; Huang, W. Effect of Molecular Weight on Conformational Characteristics of Poly(3-Hexyl Thiophene). *J. Polym. Sci., Part B: Polym. Phys.* **2017**, *55* (17), 1273–1277.

(56) Yamashita, Y.; Tsurumi, J.; Ohno, M.; Fujimoto, R.; Kumagai, S.; Kurosawa, T.; Okamoto, T.; Takeya, J.; Watanabe, S. Efficient Molecular Doping of Polymeric Semiconductors Driven by Anion Exchange. *Nature* **2019**, *572* (7771), 634–638.

(57) Murrey, T. L.; Riley, M. A.; Gonel, G.; Antonio, D. D.; Filardi, L.; Shevchenko, N.; Mascal, M.; Moulé, A. J. Anion Exchange Doping: Tuning Equilibrium to Increase Doping Efficiency in Semiconducting Polymers. *J. Phys. Chem. Lett.* **2021**, *12* (4), 1284–1289.

(58) Gann, E.; Collins, B. A.; Tang, M.; Tumbleston, J. R.; Mukherjee, S.; Ade, H. Origins of Polarization-Dependent Anisotropic X-Ray Scattering from Organic Thin Films. *J. Synchrotron Rad.* **2016**, *23* (1), 219–227.

(59) Collins, B. A.; Cochran, J. E.; Yan, H.; Gann, E.; Hub, C.; Fink, R.; Wang, C.; Schuettfort, T.; McNeill, C. R.; Chabinyc, M. L.; et al. Polarized X-Ray Scattering Reveals Non-Crystalline Orientational Ordering in Organic Films. *Nat. Mater.* **2012**, *11* (6), 536–543.

(60) Gann, E.; Collins, B. A.; Tang, M.; Tumbleston, J. R.; Mukherjee, S.; Ade, H. Origins of Polarization-Dependent Anisotropic X-Ray Scattering from Organic Thin Films. *J. Synchrotron Rad.* **2016**, *23* (1), 219–227.

(61) Wang, C.-H.; Mukherjee, S.; Maidul Islam, A. K. M.; Yang, Y.-W.; Mukherjee, M. Role of Interfacial Interaction in Orientation of Poly(N-Isopropylacrylamide) Chains on Silicon Substrate. *Macromolecules* **2011**, *44* (14), 5750−5757.

(62) O'Connor, B.; Kline, R. J.; Conrad, B. R.; Richter, L. J.; Gundlach, D.; Toney, M. F.; DeLongchamp, D. M. Anisotropic Structure and Charge Transport in Highly Strain-Aligned Regioregular Poly(3-Hexylthiophene). *Adv. Funct. Mater.* **2011**, *21* (19), 3697−3705.

(63) Chaney, T. P.; Levin, A. J.; Schneider, S. A.; Toney, M. F. Scattering Techniques for Mixed Donor−Acceptor Characterization in Organic Photovoltaics. *Mater. Horiz.* **2022**, *9* (1), 43−60.

(64) Ferron, T.; Pope, M.; Collins, B. A. Spectral Analysis for Resonant Soft X-Ray Scattering Enables Measurement of Interfacial Width in 3D Organic Nanostructures. *Phys. Rev. Lett.* **2017**, *119* (16), 167801.

(65) Collins, B. A.; Ade, H. Quantitative Compositional Analysis of Organic Thin Films Using Transmission NEXAFS Spectroscopy in an X-Ray Microscope. *J. Electron Spectrosc. Relat. Phenom.* **2012**, *185* (5−7), 119−128.

(66) Watts, B.; Swaraj, S.; Nordlund, D.; Lüning, J.; Ade, H. Calibrated NEXAFS Spectra of Common Conjugated Polymers. *J. Chem. Phys.* **2011**, *134* (2), 024702.

(67) Nahid, M. M.; Gann, E.; Thomsen, L.; McNeill, C. R. NEXAFS Spectroscopy of Conjugated Polymers. *Eur. Polym. J.* **2016**, *81*, 532−554.

(68) Hamidi-Sakr, A.; Biniek, L.; Bantignies, J.-L.; Maurin, D.; Herrmann, L.; Leclerc, N.; Lévêque, P.; Vijayakumar, V.; Zimmermann, N.; Brinkmann, M. A Versatile Method to Fabricate Highly In-Plane Aligned Conducting Polymer Films with Anisotropic Charge Transport and Thermoelectric Properties: The Key Role of Alkyl Side Chain Layers on the Doping Mechanism. *Adv. Funct. Mater.* **2017**, *27* (25), 1700173.

(69) Akepati, S. V. R.; Gupta, N.; Jayaraman, A. Computational Reverse Engineering Analysis of the Scattering Experiment Method for Interpretation of 2D Small-Angle Scattering Profiles (CREASE-2D). *JACS Au* **2024**, *4* (4), 1570−1582.

(70) Abdo, E. E.; Grundy, L. S.; Galluzzo, M. D.; Loo, W. S.; Fong, A. Y.; Takacs, C. J.; Balsara, N. P. Cylinder-Gyroid Phase Transition in a Block Copolymer Electrolyte Induced by Ionic Current. *Macromolecules* **2024**, *57* (2), 503−513.

(71) Young, N. P.; Devaux, D.; Khurana, R.; Coates, G. W.; Balsara, N. P. Investigating Polypropylene-Poly(Ethylene Oxide)-Polypropylene Triblock Copolymers as Solid Polymer Electrolytes for Lithium Batteries. *Solid State Ionics* **2014**, *263*, 87−94.

(72) Cordova, I. A.; Wang, C.; Weber, A. Z.; Segalman, R. A.; Brady, M. A.; Su, G. M. Operando Resonant Soft X-Ray Scattering As a Spatio-Chemical Characterization Technique for Electrochemistry. *Electrochem. Soc. Meet. Abstr.* **2016**, *MA2016-02* (38), 2350.

(73) Rongpipi, S.; Chan, J. M.; Bird, A.; Freychet, G.; Kusoglu, A.; Su, G. M. Revealing Mesoscale Ionomer Membrane Structure by Tender Resonant X-Ray Scattering. *ACS Appl. Polym. Mater.* **2024**.

(74) Su, G. M.; White, W.; Renna, L. A.; Feng, J.; Ardo, S.; Wang, C. Photoacid-Modified Nafion Membrane Morphology Determined by Resonant X-Ray Scattering and Spectroscopy. *ACS Macro Lett.* **2019**, *8* (10), 1353−1359.

(75) Zhong, W.; Zhang, M.; Freychet, G.; Su, G. M.; Ying, L.; Huang, F.; Cao, Y.; Zhang, Y.; Wang, C.; Liu, F. Decoupling Complex Multi-Length-Scale Morphology in Non-Fullerene Photovoltaics with Nitrogen K-Edge Resonant Soft X-Ray Scattering. *Adv. Mater.* **2022**, *34* (6), 2107316.

(76) Jiao, X.; Ye, L.; Ade, H. Quantitative Morphology−Performance Correlations in Organic Solar Cells: Insights from Soft X-Ray Scattering. *Adv. Ener. Mater.* **2017**, *7* (18), 1700084.

(77) Quill, T. J.; LeCroy, G.; Halat, D. M.; Sheelamanthula, R.; Marks, A.; Grundy, L. S.; McCulloch, I.; Reimer, J. A.; Balsara, N. P.; Giovannitti, A.; et al. An Ordered, Self-Assembled Nanocomposite with Efficient Electronic and Ionic Transport. *Nat. Mater.* **2023**, *22* (3), 362−368.